

Deep learning architecture for sparse and noisy turbulent flow data

Filippos Sofos (Φίλιππος Σοφός),^{1,2} Dimitris Drikakis (Δημήτρης Δρικόκης),^{1,a)} and Ioannis William Kokkinakis (Ιωάννης Κοκκινάκης)¹

¹⁾*Institute for Advanced Modeling and Simulation, University of Nicosia, Nicosia CY-2417, Cyprus*

²⁾*Condensed Matter Physics Laboratory, Department of Physics, University of Thessaly, Lamia 35100, Greece*

The success of deep learning models in fluid dynamics applications will depend on their ability to handle sparse and noisy data accurately. This paper concerns the development of a deep learning model for reconstructing turbulent flow images from low-resolution counterparts encompassing noise. The flow is incompressible through a symmetric, sudden expansion featuring bifurcation, instabilities and turbulence. The deep learning model is based on convolutional neural networks, in a high-performance, lightweight architecture. The training is performed by finding correlations between high- and low-resolution two-dimensional images. The study also investigates how to remove noise from flow images after training the model with high-resolution and noisy images. In such flow images, the turbulent velocity field is represented by significant color variations. The model's peak signal-to-noise ratio is 45, one of the largest achieved for such problems. Fine-grained resolution can be achieved using sparse data at a fraction of the time required by large-eddy and direct numerical simulation methods. Considering its accuracy and lightweight architecture, the proposed model provides an alternative when repetitive experiments are complex and only a small amount of noisy data is available.

I. INTRODUCTION

Super-resolution (SR) deep learning models have extensively been used in computer vision applications¹, and more recently in fluid dynamics; see² for a recent review. Super-resolution can advance experimental^{3,4} and computational fluid dynamics (CFD) research.^{5,6}

In experiments, cameras can be used to obtain spatiotemporal flow images.⁷ In numerical simulations, SR can be used to upscale low-resolution (LR) images into high-resolution (HR), enhancing the spatial and temporal resolution in two-dimensional (2D) and three-dimensional (3D) flow simulations.⁸⁻¹² This can reduce the need to perform computationally demanding large and complex numerical simulations.

Despite the SRs' potential to contribute to fluid dynamics research and applications, several areas regarding the performance of the SR architectures deserve further study, particularly the datasets' effects of sparsity and noise.^{2,13-15} Sparsity is a common factor in most applications¹⁶, as it is more likely limited experimental data will be available and numerical simulations are often under-resolved. Noise can be present in imaging obtained in laboratory and field experiments. For example, noise may occur during the image acquisition process due to low incoming radiation, image blur due to movement, or even hardware misfits that affect the obtained result.¹⁷ That sparsity and noise can significantly affect DL model training, as a recent study showed.¹⁸ Efforts to diminish noise in DL models have been presented in the literature.^{19,20}

Deep learning architectures are usually constructed by consecutive neural network (NN) layers²¹, properly interconnected to embed non-linear mathematical equations. In hardware terms, NN nodes are usually built on parallel cores (e.g.,

Graphical Processing Units - GPU), with the aid of software backbones based on TensorFlow²², Keras²³, and PyTorch²⁴, most of the times. Common NN architectures for super-resolution can be categorized according to the increasing complexity; see the survey by Anwar, Khan, and Barnes²⁵:

- Linear networks, with feed-forward calculations only.
- Residual networks, where skip connections are formed between different network layers.
- Recursive networks, which employ recursively connected layers.
- Progressive recursive networks that provide the output in more than one step.
- Densely connected networks, where the output is usually connected to previous layers, back-propagating or with residual connections.
- Multi-branch networks, where different branches function in parallel and re-combine at the end to give richer image representations.
- Attention-based networks, selective in a way that focuses on features significantly affecting the SR result only.
- Multiple-degradation handling networks that consider other image degradation methods as inputs rather than bicubic degradation that the other models do
- Generative adversarial networks (GANs), where a generator and a discriminator network are created. The generator creates images, and the discriminator tries to find if these are real or artificial, selecting the best result each time.

The above architectures have been widely incorporated in computer vision and image classification applications. One can refer to the survey of Wang, Chen, and Hoi²⁶ for a detailed analysis of such methods and relevant datasets.

An example of a fully operational architecture is the U-Net²⁷, which has been employed as the base design network for imaging applications such as super-resolution, image segmentation, and image encryption, outperforming similar but more complex ones (e.g., U-Net⁺⁺ and V-Net).²⁸ In many

^{a)}Electronic mail: Author to whom correspondence should be addressed:drikakis.d@unic.ac.cy

of these approaches, bicubic or deconvolution techniques are employed for up-sampling images. Some inherent problems in these traditional methods include low performance in the up-sampling of small-sized images and a low-pass filtering behavior, leading to the loss of high-frequency information and the blurring of image edges.

Increased reconstruction performance is also achieved by considering skip connections between the U-type layers, from the first layers, where information is richer, to the final layers responsible for the reconstruction in the ResNet.²⁹ All these architectures have been incorporated into various applications, from classical image processing^{30–32} to speech recognition³³ and flow reconstruction.^{6,26,34–36} At present, cutting-edge approaches for image reconstruction have moved to more complex architectures, such as GANs³⁷. Notwithstanding their effectiveness, GANs may be in cases prone to over-fitting³⁸, as U-Net-based architectures as well³⁹, while the generated images may have an over-repaired sense of unreality.⁴⁰ The main problem, though, is the increased computational cost, compared to U-Net based architectures, that makes their use unpractical for lightweight applications.

The flow in question is a turbulent flow through a sudden expansion geometry commonly encountered in hydraulics, medical applications, mechanics, microjets, heat exchangers, nuclear applications, oil and gas extraction, combustion, and air ducts.^{41–44} Planar sudden expansion flows are fascinating examples of asymmetric and complex unstable flow physics even when the geometry is fully symmetric.⁴⁵ This behavior could be ascribed to the Coanda effect⁴⁶, but the exact mechanism is still not fully understood despite many years of research. Suddenly, expanded flows remain symmetric up to a certain Reynolds number, Re , with two recirculation regions of equal length formed on either side of the expanding channel. As the Re increases, the flow becomes asymmetric about its centerline and separation regions of unequal length arise and remain in the flow field even up to high Reynolds numbers.

Several studies were performed in the laminar flow regime, including numerical and experimental investigations.^{45,47,48} Moallemi et al.⁴⁹ showed using DNS that bifurcation initiates at higher Reynolds numbers as the expansion ratio decreases. Karantonis et al.⁵⁰ performed implicit Large Eddy Simulations at high Reynolds numbers and comparisons with experimental measurements. The authors investigated the structure of the separated regions, turbulence structures – through the Reynolds stress anisotropy componentality – and turbulence kinetic energy budgets. The results revealed that compressibility influences particular flow physics and a great deal of complexity within the asymmetric regions downstream of the expansion.

In this paper, we implement a super-resolution architecture called Deep Learning Flow Image (DELFI), based on a simple and practical U-Net structure²⁷ capable of running fast even in standard computer hardware. The sudden expansion flow setup of the past experimental and computational studies^{50,51} has been employed to investigate the DELFI model and assess its performance in reconstructing blurred (pixelated) and noisy flow fields with asymmetries, turbulence and separa-

tion. DELFI is investigated for its ability to process both pixelated and noisy images, which fundamentally involve different distortions. While blurred image pixels (i.e., from a sparse field) spread over their neighbourhood, making it harder to distinguish between flow details, noise causes random variations in pixel values without altering the spatial image features. Nonetheless, we show that DELFI can successfully reconstruct the flow field in both distortion cases over a wide range of downscaled images and different levels of Gaussian and uniform noise, which, to our knowledge, has not been shown to such an extent before. Quantitatively, the derived peak signal-to-noise (PSNR) ratio reaches $PSNR \approx 45.0$, a top-performing value in the field.

Therefore, the proposed architecture and its ease of implementation can be employed in practical engineering problems after being trained from scratch with only a small amount of input images or used as a pre-trained model through a transfer learning approach. In the following Sections, the employed CFD dataset is presented, the DL architecture components are described, training/testing details are given, and the model's results for pixelated and noisy data are analyzed. Finally, a comparison and discussion on existing architectures are made, and future research directions are given.

II. MODELS AND METHODS

A. CFD model and turbulent flow setup

The data for investigating the DELFI's model performance concerns a turbulent flow through a suddenly-expanded channel. The CFD model and its validation were presented in a previous study.⁵⁰ A summary of the model and the data is given below.

The flow case corresponds to a relatively high Reynolds number of 10,000, based on the inlet bulk velocity and the step height of the channel (h) to investigate the asymmetric flow.⁵¹ The Mach number based on the bulk velocity at the channel inlet is 0.1, which, after expansion, is reduced by one-third. Figure 1 shows a schematic of the sudden expansion, which comprises two channels, each of a different height. The flow domain consists of an inlet channel of height h and a downstream channel of height $H = 3h$, resulting in an expansion rate ($ER = H/h$) 3. The characteristic length of the channel is the step height, h , with a value of 1. The total length of the domain is $84h$. The inlet and downstream channels have lengths of $4h$ and $80h$, respectively. These particular geometrical features were chosen to ensure that the flow (a) is fully developed (turbulent) before reaching the expansion step and (b) the buffer layer at the end of the domain has damped unsteadiness in the flow before exiting the domain. Finally, the aspect ratio ($AR = W/h$) of the channel inlet section is 5. An illustration of the three-dimensional turbulent flow field is provided in Fig. 2.

The simulations were performed using the block-structured grid code CNS3D, which solves the Navier-Stokes equations using the finite-volume method (FVM). CNS3D can be used for implicit Large Eddy Simulations (ILES) and DNS. The

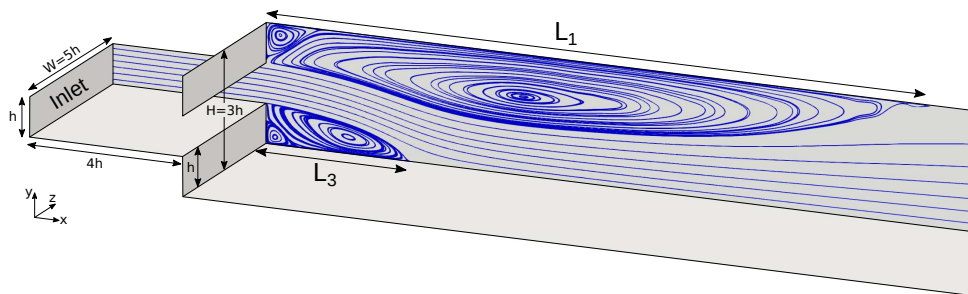


FIG. 1. Illustration of the planar sudden expansion (PSE) configuration. Streamlines of the mean velocity depict the asymmetric flow bifurcation and the recirculation bubbles.

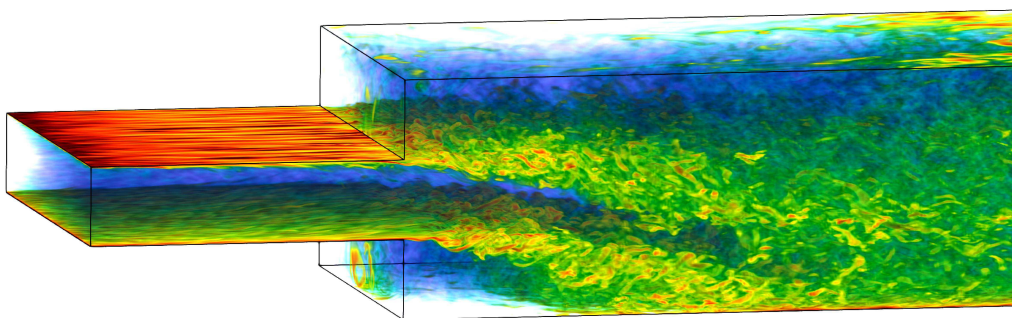


FIG. 2. Contour plot of the vorticity magnitude illustrating the flow asymmetry, turbulent boundary and shear layers.

advective terms are solved using the Godunov-type (upwind) method, whose inter-cell numerical fluxes are calculated by solving the Riemann problem using the reconstructed values of the primitive variables at the cell interfaces. A one-dimensional swept unidirectional stencil is used for the spatial reconstruction. The numerical simulations herein were obtained using an augmented 11th-order WENO scheme⁵² for interpolation in conjunction with the approximate HLLC Riemann solver.⁵³ The solution is advanced in time using an explicit five-stage (fourth-order accurate) optimal strong-stability-preserving Runge-Kutta method⁵⁴. Further details of the numerical aspects of the code can be found in past literature^{52,55} and references therein.

A synthetic turbulent boundary condition based on the digital filter (DF) technique was also implemented at the inlet.^{56,57} The DF approach produces a velocity signal in three directions by matching ad hoc first- and second-order statistical moments, length and time scales, and energy spectra. We selected the DF approach for generating artificial inflow data as the filtering operation was applied only in 2D (rather than 3D), making the whole process much faster and computationally efficient. A buffer layer was employed at the outflow to avoid any numerical reflections. Standard no-slip, viscous, and adiabatic wall boundary conditions were assigned to the

boundary surfaces in the wall-normal (y) direction. Periodic conditions were chosen for the boundary surfaces normal to the spanwise (z) direction.

CNS3D produced the turbulent data in the wall-resolved implicit large eddy simulation (ILES) framework. The mesh spacing (Δy) was scaled using the conventional inner variable method $\Delta y^+ = u_\tau \Delta y / \nu_w$, where $u_\tau = \sqrt{\tau_w / \rho_w}$ is the friction velocity, ν_w , τ_w and ρ_w are the near-wall kinematic viscosity, wall shear-stress, and density, respectively⁵⁸. The grid resolution at the channel inlet in the streamwise, wall-normal and spanwise directions is $\Delta x^+ \simeq 26$, $y_w^+ = 1$ (corresponding to $y^+ = 0.5$ in the first cell-centre off the wall), and $\Delta z^+ \simeq 15$, respectively. At the expansion corner, $\Delta x^+ \approx y_w^+$. The grid gradually coarsens towards the exit boundary, reaching approximately a value of $\Delta x^+ \simeq 50$ at the expected $L_1 \simeq 14.4h$ (location of upper recirculation layer re-attachment). After that, it increases linearly towards the outlet, eventually reaching a value of $\Delta x^+ \simeq 180$. In total, the computational domain contains 34,810,000 cells. The grid resolution and numerical scheme yielded accurate results⁵⁵ for wall-bounded turbulent flows at low Mach numbers. The present fine mesh corresponds to wall-resolved ILES following typical resolution recommendations for LES and DNS simulations^{59–61}.

The total simulation time was $300h/U_B$, from which statis-

tics were obtained over the last $100h/U_B$, where U_B is the bulk velocity of the channel inlet, and h is its height. Over the statistics period, 407 images of the 2D surface contour plot of the streamwise velocity are extracted at a constant time interval. The above is carried out at three equidistant z -normal (xy) planes, namely at $z/h = 1.0, 2.5,$ and 4.5 , to enhance the image sample size further. Thus, a total of 1,221 images are available for the present study.

B. Deep Learning Flow Image Model

The proposed image reconstruction architecture (DELFI) is based on convolution operations and implemented in TensorFlow.²² Convolutional Neural Networks (CNN) are widely incorporated in computer vision applications⁶² and, recently, they have found application in fluid flow investigation, such as turbulence, as they can extract complex spatial patterns.⁶³ One of the main features distinguishing CNNs from classical Artificial Neural Networks (ANNs) is their sparse interactions between inputs and outputs, resulting in lower computational burden and memory requirements, making them appropriate for dealing with big data applications and complex fluid-related tasks.⁶⁴

CNN involve operations such as convolution, deconvolution, average and max pooling, and batch normalization⁶⁵, functioning in layers according to the flow of information. For 2D data, e.g., images, the input layer accepts the data as an array of pixel values in 3 layers in color images (RGB image) or one layer (grayscale image). Pixel values represent a property of interest. In this paper, pixels denote velocity values. These values, before processing, are normalized between 0 and 1 to increase the network's generalization ability and prevent issues associated with biases during calculations.

As per the flowchart presented in Fig. 3, the model accepts an LR image set of dimensions $(W/n \times H/n \times 3)$ as the training set, along with the respective high-quality image set (HR) of sizes $(W \times H \times 3)$, which serves as the ground truth⁶⁶. Flow images are pre-processed so the correct dimensions are fed to the model. To make the comparison between HR and LR images possible, they must be of the same dimension. At first, the LR set is resized through linear interpolation techniques to $(W \times H \times 3)$ adhere to HR dimensions.

Next, the image passes through consecutive CNN layers representing the multichannel feature maps²⁷. The first layer is convolutional (TensorFlow Conv2D function) with 64 filters, where each filter detects specific image patterns within different frequency ranges. These filters are created with a convolutional kernel, a 3×3 array, applying on consecutive input image regions, followed by a ReLU activation function⁶⁷. Information from the first CNN layer is transferred to a second CNN layer, with 64 filters and a ReLU function on the output. These two CNN layers consist of the contraction mechanism of DELFI. During deconvolution (expansion path), residual information is added directly from the input image to restore possible losses, and a deconvolution layer (TensorFlow Conv2DTranspose function) follows. The final layer gathers all filters to an image with dimensions

$(W \times H \times 3)$. This is the reconstructed output. During this process, the image size is not altered by appropriately setting the strides and padding parameters, e.g., $\text{strides}=1$ and $\text{padding}=\text{zero}$. The features of DELFI and its performance compared to similar architectures are also discussed in Sec. § III C.

C. Training and Testing Data

The HR dataset contains 1221 randomly divided into 976 training images and 245 testing images. Training images are fed into the model, and testing images are kept for post-processing to ensure the model works fine when unseen images are fed. The model is trained both with LR (pixelated) and noisy images. The first step includes six image sets of various resolutions to train and validate the constructed computational model. The LR images are produced by dividing the HR image dimensions by a scale factor of n , where $n = 2, 4, 6, 8, 10, 12$, giving six LR sets, LR1, LR2, LR3, LR4, LR5, and LR6, respectively. This process reduces image dimensions (see Table 1) and has been widely incorporated to train similar image reconstruction models⁶⁸⁻⁷⁰. To proceed in image reconstruction and be able to compare with the ground truth images, the LR images are resized back to the original dimensions through linear interpolation (Fig. 3a). In such a way, the final LR sets are pixelated instances of the respective HR images. They can be considered physical equivalents produced by DNS simulations on sparse grids.

Another training instance employs images with added noise, which resembles real experimental procedures. This paper examines the effects of Gaussian and uniform noise.⁷¹ When Gaussian noise is added to an RGB (Red, Green, Blue) image, it introduces random variations in pixel values, corresponding to the case of images captured in low-light conditions or with electronic sensors that introduce noise. The Gaussian noise $f_g(x)$ depends on the noise amplitude and is given by⁷²:

$$f_g(x) = \frac{1}{\sigma\sqrt{2\pi}} \exp\left(-\frac{(x-\mu)^2}{2 \cdot \sigma^2}\right) \quad (1)$$

where μ is the mean, σ the standard deviation, and x denotes the deviation from the mean. In the case of uniform noise $f_u(x)$, it follows a uniform distribution, creating a more constant level of randomness, resembling sensor artifacts or imperfections in imaging devices, as⁷³:

$$f_u(x) = \frac{1}{2\sigma} \quad (2)$$

where x is the random variable that can take on values between σ and $-\sigma$.

III. RESULTS

The computational fluid dynamics results employed in the present study had been extensively examined and compared to

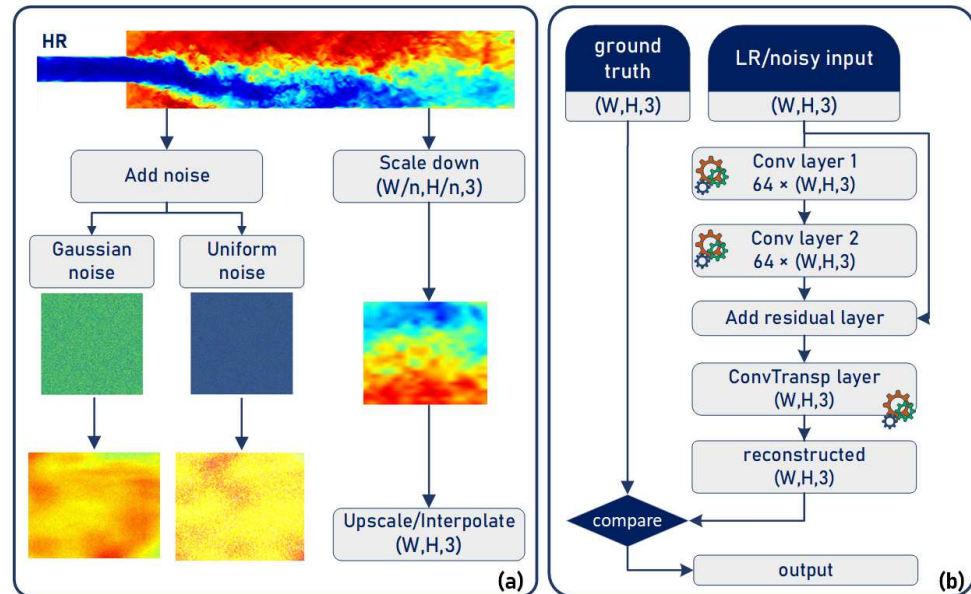


FIG. 3. (a) Flow image pre-processing, where LR, Gaussian and uniform (white noise) image sets are constructed for model training and testing. Random regions of the HR image are shown. (b) The proposed architecture. The model accepts LR or noisy input images and reconstructs flow characteristics into a higher resolution counterpart, the predicted image. The HR images are employed as the ground truth and are compared to the predicted images.

TABLE I. Dimensions of training/testing images, derived from the original high-resolution image input(s), i.e., the ground truth images, for which $(W \times H \times N) = (2296 \times 325 \times 3)$. Each image is given in RGB format, i.e., in three channels ($N = 3$).

Resolution	LR1	LR2	LR3	LR4	LR5	LR6
Dimensions	$1148 \times 162 \times 3$	$574 \times 81 \times 3$	$382 \times 54 \times 3$	$287 \times 40 \times 3$	$229 \times 32 \times 3$	$191 \times 27 \times 3$

the literature previously⁵⁰. One of the key indicators used in sudden expansion flows is the locations of the separation and reattachment of the recirculation bubbles that form. The reattachment lengths (x_R) found in the literature of planar sudden expansion (PSE) flows along with the corresponding geometrical properties are all summarized and presented in Table II. Note that there are slight differences in the geometric and/or flow properties between the various experimental and numerical studies referenced, which cause the differences in the reattachment lengths quoted.

A. Super Resolution

DELFI is individually trained with six image sets of various resolutions (Fig. 3), creating six different model instances. Results are examined and analyzed on these instances, named LR1-LR6, with the name corresponding to the respective in-

put image resolution used for training (LR1 to LR6, see Table I). During every computational time step, the input LR image is first linearly interpolated to higher dimensions to comply with the HR basis of comparison, i.e., $2296 \times 325 \times 3$.

Imaging applications employ the peak signal-to-noise ratio ($PSNR$) metric to assess the quality of reconstruction.⁷⁸ The $PSNR$ for the i^{th} image in an image set is given by:

$$PSNR_i = 20 \log \left(\frac{1}{\sqrt{MSE(HR_i, REC_i)}} \right) \quad (3)$$

where HR is the high-resolution and REC is the reconstructed image. A higher $PSNR$ value represents a better reconstruction.

The average $PSNR$ is calculated for all model instances, and the results are presented in Fig. 4. Each model has been trained with the respective image set; for example, the LR1 instance has been trained with LR1 images, the LR2 time instance with LR2 images, and so forth. During testing, where

TABLE II. Literature review on the primary reattachment lengths of a turbulent planar sudden expansion flow. [†]Study from which flow results are taken to create the high-resolution images.

Author(s)	$Re (\times 10^4)$	$ER (H/h)$	$AR (W/h)$	U_{inlet} profile	$L_1, L_3 (h)$
Abbott and Kline ⁷⁴	2-5	1.125-5	2-16	Fully developed	11-15, 3.5-4
Mehta ⁷⁵	12.5	3	0.25	Fully developed	15, 4.5
Aloui and Souhar ⁴⁴	3.2	2.27	0.18	Fully developed	10.8, 5.4
De Zilwa, Khezzar, and Whitelaw ⁷⁶	2.65	2.86	12.31	Uniform	17, 3.4
Escudier, Oliveira, and Poole ⁷⁷	5.55	4	5.33	Uniform	11.5, 3.13
Casarsa and Giannattasio ⁵¹	1	3	10	Fully developed	14.38, 3.68
Karantonis <i>et al.</i> ^{50,†}	1	3	5	Fully developed	16.57, 3.82

the models reconstruct an image from an unseen dataset, all image sets, from LR1 to LR6, are fed into each model instance, and the $PSNR$ values are tabulated. The highest $PSNR$ is obtained for the LR1 model when the testing input is of LR1 resolution, i.e., only with a slight blurring compared to the ground truth. However, from a broader point of view, this fails to reconstruct images of lower resolutions, especially for LR3 to LR6, since the $PSNR$ values here are relatively small.

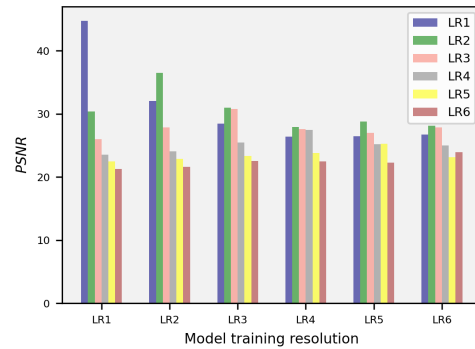


FIG. 4. Values of $PSNR$ for all LR1-LR6 model instances employed. The models are trained with their respective image resolution and validated with all available LR images. Different colors correspond to different testing inputs, according to the legend.

The LR2 (trained with LR2 resolution) performs fairly well when LR1 and LR2 inputs are to be reconstructed to their refined counterparts. The LR3 performs equally well for LR2 and LR3 inputs but fails in more pixelated images. It is also shown that LR4, LR5, and LR6 perform similarly for all input resolutions. Another point worth mentioning is that LR5 and LR6 trained models have given higher $PSNR$ when the inputs are of LR1-LR3 resolution compared to LR5-LR6 inputs. It seems that these models, although being trained with very low-resolution inputs, can perform relatively well on reconstructing less pixelated images. This is evidence of low (or not at all) over-fitting since the model is not bound only to effective LR5 and LR6 image reconstruction and can perform equally well outside this resolution range.

Some more general remarks can also be derived from Fig.

4. First, it is evident that models trained only with lower image resolution images, such as LR4-LR6, cannot be employed on high-performance applications. Second, all model time instances except LR1 perform well when asked to reconstruct an image of LR2 resolution. LR2 images are of dimension $(W/4 \times H/4 \times 3)$, i.e., four times smaller than the fine input of $(W \times H \times 3)$. This reveals that when a sparse simulation grid is employed, four times smaller than the respective accurate DNS grid, the proposed model is capable of bypassing the inherent computational complexity and excess time needed for DNS simulations by considering a sparser grid and feeding the results into the DELFI reconstruction model.

To view the error induced during reconstruction, error heat maps are extracted for a sample HR/REC couple. The absolute difference between the images is calculated for every i^th pixel, as $Diff. = |HR_i - REC_i|$. Figure 5 presents the errors produced after reconstructing an example image of LR1-LR6 resolution. The errors are practically zero for LR1 and remain low for LR2 (Figs. 5a and b). The error increases in the LR3 case (Fig. 5c), reaching about 30% in regions where high-velocity values from the input jet combine with low-velocity regions. These include the boundary before the contraction and the internal line that follows the jet development inside the contracted area. As expected, the error increases for LR4, LR5, and LR6 in Figs. 5d, e, and f, respectively, since the reconstruction performance for DELFI is lower in these cases, as also seen from the $PSNR$ values in Fig. 4.

Furthermore, the calculated $PSNR$ values shown in Figs. 4 are verified by presenting specific regions from the flow field and their similarity to the refined image prototype. Four different areas from the flow field are selected for presentation, i.e., Region 1 after the expansion input, Region 2 on the top where the jet meets the boundary, Region 3 on the bottom limit of the jet where the flow begins to stabilize, and Region 4 towards the outlet. These regions, for three random time instances, are shown in Fig. 6

The model instances trained and validated with LR1 (which have given the highest $PSNR$), LR2, and LR3 images are presented in Fig. 7. The four regions are numbered (1 to 4), and the LR and the reconstructed super-resolution image (henceforth labeled as SR) are given for every instance. The HR regions are also shown for comparison. LR1 images are slightly blurred, and the reconstructed image sections (Fig. 7c) present very close similarity to the respective ground truth regions.

This is the author's peer reviewed, accepted manuscript. However, the online version of record will be different from this version once it has been copyedited and typeset.

PLEASE CITE THIS ARTICLE AS DOI: 10.1063/1.50200167

Preprint

7

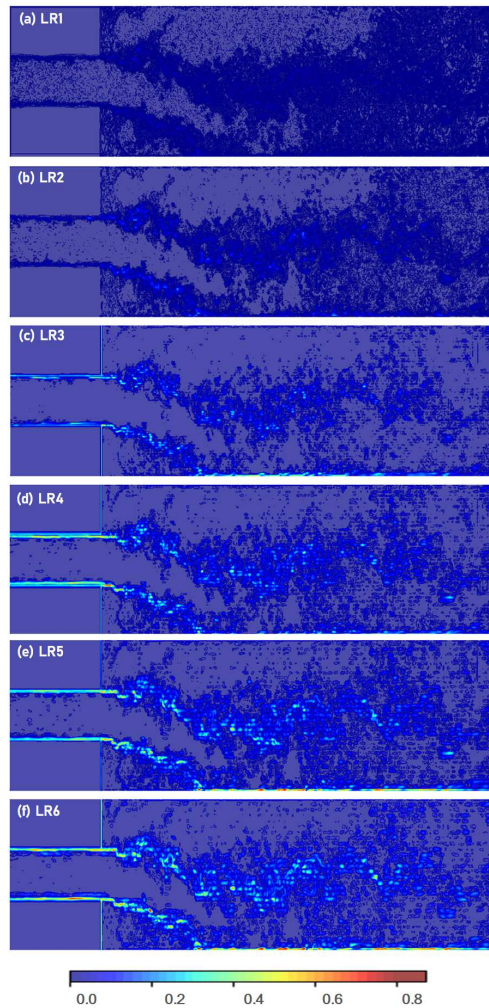


FIG. 5. Error heat maps, denoting the difference between an example HR image and reconstructed images, resulting from an input resolution of (a) LR1, (b) LR2, (c) LR3, (d) LR4, (e) LR5, and (f) LR6.

This instance achieved $PSNR = 42.75$. When trained and validated with LR2 images, the model also gives high $PSNR$. The SR counterparts recover small color regions of the flow; see, for example, Fig. 7e.1, and de-blurring the edges when needed (Fig. 7e.4). The LR3 instance also results in a good reconstruction (Fig. 7g). However, training with a resolution that scales below 8 (e.g., LR4-LR6) has not accurately reproduced the ground truth images.

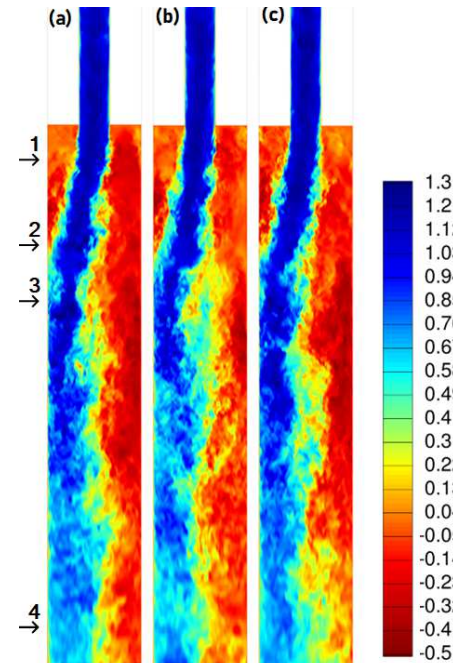


FIG. 6. Various time instances of the velocity flow field and four different regions in which the super-resolution is focused, in (a) the beginning of the flow, (b) in an intermediate time step, and (c) near the end of the flow. Arrows indicate the cross-sections where velocity profiles have been extracted.

B. Noise Reduction

The second step incorporates adding Gaussian and uniform noise patterns to the HR image. Image pixels have values normalized within 0 – 1. Various Gaussian noise patterns are examined, with mean values $\mu = 0.0$ and standard deviations in the range $\sigma = [0.025, 0.05, 0.075, 0.1]$. Uniform noise levels tested refer to constant values of noise being added on each pixel within levels, l , as $l = [0.1, 0.2, 0.3, 0.4, 0.5]$.

The obtained $PSNR$ is given in Fig. 8. Uniform noise levels are added to the respective HR images (Fig. 8a). Remarkable performance is achieved for all investigated cases, with the highest $PSNR = 42.76$ obtained for $l = 0.1$, while $PSNR = 34.83$ is obtained for $l = 0.5$, although degradation is significant at such level. Regarding the Gaussian noise instances (Fig. 8b) starting from a distribution with $\mu = 0.0$ and $\sigma = 0.025$, $PSNR = 38.35$ is obtained. The performance falls by considering a distribution with $\sigma = 0.075$, as $PSNR = 17.56$.

Regarding the reconstruction error, Fig. 9 presents the heat maps for a uniform noise reduction process for various noise levels. Noise reduction is successful in most regions inside the

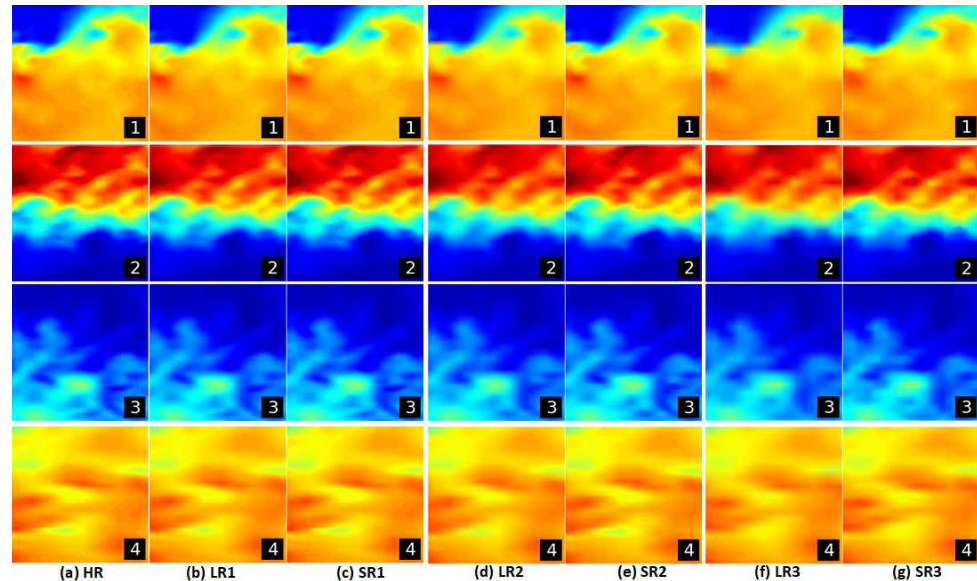


FIG. 7. Flow reconstruction results when the model is trained and validated with LR1-type images. (a) The ground truth regions of HR resolution are used for reference, and the respective (b) LR1, (c) LR1 reconstructed, (d) LR2, (e) LR2 reconstructed, (f) LR3, (g) LR3 reconstructed.

channel, except for regions where high-velocity values from the input jet combine with low-velocity regions, as was also observed in Fig. 5. Nevertheless, error values for $l = 0.1 - 0.5$ remain below 15% for all cases investigated.

The four image regions before and after reconstruction are also presented for various noise levels. Figure 10 shows the HR, the uniform-noise region (UNR) for $l = 0.1$ (UNR-0.1), and the respective reconstructed image, SR-0.1. The reconstructed result is very close to the ground truth. Even when increasing the noise level to $l = 0.3$ (Fig. 10d), the model reconstructs the fields efficiently (Fig. 10e). The highest noise effect investigated here, at $l = 0.5$, has given significant image degradation in Fig. 10f. Nevertheless, the reconstructed result (Fig. 10g) is still very close to the HR counterpart.

When Gaussian-type noise is added to the flow images, the effect is more prominent, and reconstruction achieves slightly lower metrics than the uniform noise instances, at least in the noise level range examined here. The reconstruction error in Fig. 11 reaches 15% in many regions inside the contracted area, especially for $GNR = 0.1$ (Fig. 11d).

As for the local investigation and the respective optical result, in Fig. 12a-c, where (i) the HR, (ii) the Gaussian noise regions (GNR) for $\sigma = 0.025$ (GNR-0.025), and (iii) the reconstructed image, SR-0.025, are shown, the reconstruction method has removed the noise. A significant part of the Gaussian noise has also been removed from GNR-0.05 for the case of $\sigma = 0.05$, as evident in Fig. 12e. However, Fig. 12g shows

that for $\sigma = 0.075$, the model could not remove its effect completely.

C. Comparison with other CNN Architectures

Next, DELFT's performance will be compared with other literature models dealing with fluid-related image reconstruction (Fig. 13). All models are selected from relevant papers during 2019-2023. The main selection criterion was the existence of a fluid reconstruction method presented, along with the obtained $PSNR$ value given. We also included cases where the $L2$ norm or the MSE is given (considering $L2 \approx MSE$) and incorporated Eq. (3) to calculate $PSNR$.

The downsampled skip-connection/multi-scale (DSC/MS) architecture⁷⁹ was found to accurately reconstruct turbulent flows from coarse field images for a wide range of applications in both laminar and turbulent flows. By examining the effect of pooling layers, the average pooling was superior to max pooling in robustness. An autoencoder was also utilized for the reconstruction.⁸⁰ The autoencoder convolutional neural network (AE-CNN) consists of a CNN followed by a multi-linear perceptron (MLP) to reduce image dimensions for practical computations and an inverse architecture for the decoder, achieving similar performance to DSC/MS.

Based on the U-Net architecture, the multi-scale temporal path U-Net (MST-UNET) architecture was modified to recon-

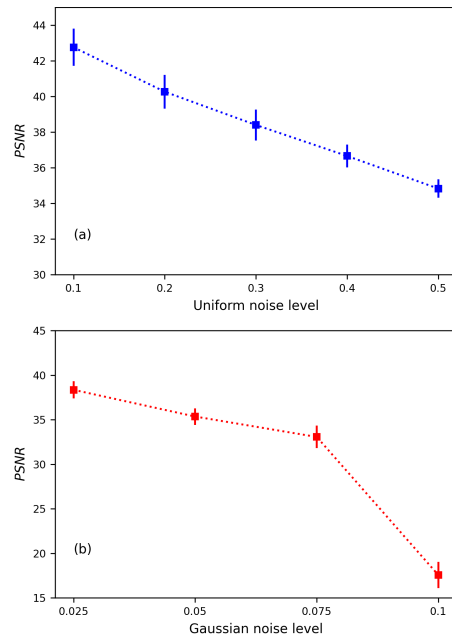


FIG. 8. Values of $PSNR$ for models with added (a) uniform and (b) Gaussian noise. Error bars denote the standard deviation. Lines are a guide to the eye.

struct both temporal and spatial fields.⁸¹ Taking into consideration the LR spatial data and combining the flow fields at various time steps as the flow proceeds, MST-UNET was found to improve prediction accuracy. Among various multi-branch network base architectures investigated by Kong *et al.*⁸², the CNN-III architecture achieved the highest $PSNR$ in a supersonic isolator flow field.

Regarding GANs, the super-resolution GAN (SRGAN)¹² was applied to increase the resolution of all fields and to extract velocity values parallel to the wall derived from shear stress and pressure measurements. The training images were taken from DNS simulations for $Re_\tau = 180$.

Jeon and You⁸³ investigated various architectures for reconstructing velocity fields from transitional boundary layers. The study included the linear super-resolution convolutional neural network (SRCNN)⁸⁴ that provided a relatively low $PSNR$, as well as the ESRGAN architecture.³⁷ The highest $PSNR$ score was reported by Kong *et al.*⁷⁸ using the multiple path super-resolution convolutional neural network (MPSRC). The super-resolution reconstruction of temperature fields gave $PSNR > 50.0$. The temperature fields investigated were relatively smooth, without extreme color variations, where even the simple SRCNN architecture achieved $PSNR \approx 47.0$.

DELFI, on the other hand, belongs to the residual networks

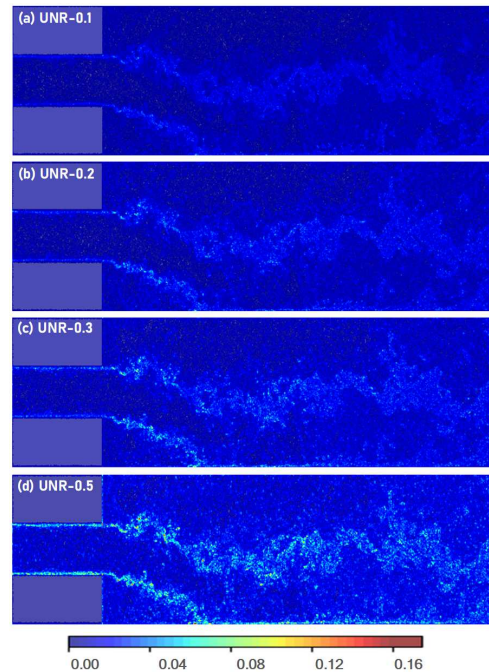


FIG. 9. Error heat maps, denoting the difference between an example HR image and reconstructed images, resulting from a noisy input with uniform noise level: (a) $l = 0.1$, (b) $l = 0.2$, (c) $l = 0.3$, (d) $l = 0.5$.

category. It employs a relatively simple architecture, with two convolutions, one deconvolution and one residual layer. As shown from the reconstruction outputs for both pixelated and noisy images (Section § III), the model provides high $PSNR$ despite its simplicity. The $PSNR \approx 45.0$ is among the highest in the literature (Fig. 13). The problem investigated here is a relatively complex flow type with significant color variations (see Fig. 6). DELFI's reconstruction performance and its simplicity in the implementation are promising for the further application of the model in various fluid flow problems.

Furthermore, DELFI has also been investigated here for its ability to reconstruct images with noise (Gaussian and uniform noise). Although there are studies for reconstructing LR images to HR, only a few refer to noise removal in fluid dynamics. For example, in Callaham, Maeda, and Brunton¹⁹, several flow systems with various noise levels were studied, and it was found that a sparse representation method recovers the HR images better than least squares regression, in which over-fitting occurred. In an unsupervised ML, the degradation and super-resolution attention architecture (D-SRA) facilitated the restoration of noisy flow fields occurring in high-speed imaging.⁸⁵ Physics-informed learning also has an ac-

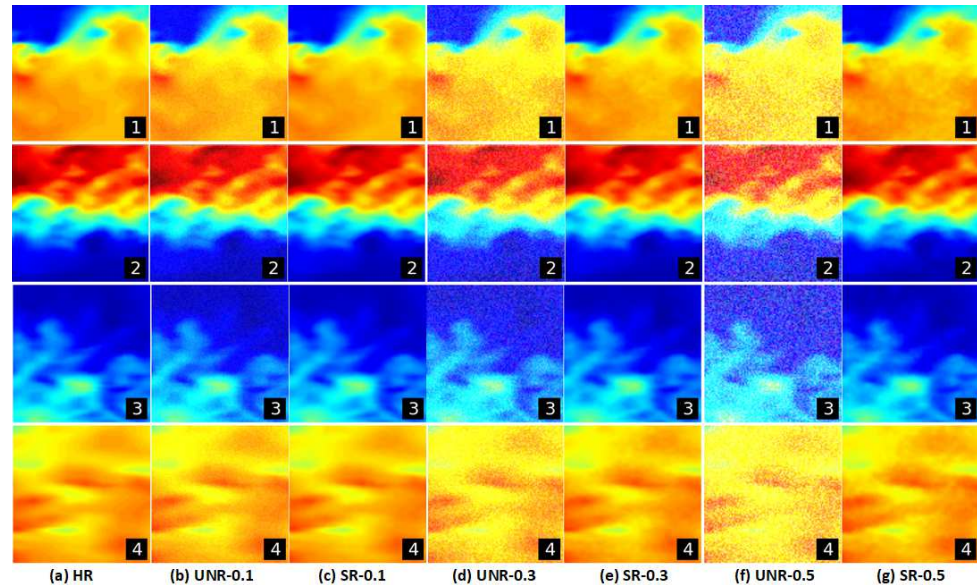


FIG. 10. Flow reconstruction result when the model is trained and validated with images with uniform noise, $l = 0.1 - 0.5$. (a) The ground truth regions of HR resolution are used for reference, and the respective (b) UNR-0.1, (c) UNR-0.1 reconstructed, (d) UNR-0.3, (e) UNR-0.3 reconstructed, (f) UNR-0.5, (g) UNR-0.5 reconstructed.

tive role in noisy image reconstruction. A physics-constrained Bayesian neural network (PC-BNN) can reconstruct the flow field when data are corrupted with measurement noise of various levels⁸⁶. The CNN super-resolution (CNN-SR) architecture⁸⁷ provided accurate results when dealing with LR inputs with Gaussian noise, non-Gaussian noise, or downsampled measurements.

IV. CONCLUSIONS

The process of training complex networks with deep learning layers has been adopted in this paper. Two-dimensional data of a bifurcating turbulent flow in a suddenly expanded channel have been employed as the test case since its inherent complexity fits well on convolutional neural network operations.

To establish a model training and testing database, the original simulation-extracted, high-resolution images are pre-processed to give low-resolution images with uniform and Gaussian noise. This approach aims to suggest a computational model that can deal with cases that resemble actual fluid experiments, where pixelated and noisy datasets are acquired and efficient post-processing and prediction tasks are the open questions. The proposed architecture, DELFI, is based on a lightweight, residual-layer construction that is easy to train and adjust to similar fluid dynamics problems. For the spe-

cific expanding channel turbulent dataset, reconstruction metrics, in terms of the peak signal-to-noise ratio, have reached $PSNR = 44.75$ for low-resolution images. The absolute error between a high resolution and a reconstructed image is kept below 15%, even when the input image is highly pixelated.

The proposed architecture has achieved $PSNR = 42.76$ for images with added uniform noise. Although noise is an indispensable component of all measurement systems, it has not been widely investigated in the super-resolution literature. DELFI has given small errors during noise reduction, below 10% for uniform noise levels $l < 0.3$ and less than 15% for higher levels. These errors appear only in small regions inside the flow field where velocity values present abrupt changes. Higher error values have been obtained during Gaussian noise removal, where errors appear in more regions inside the contracted channel, especially for noise distribution with a standard deviation equal to 0.1. However, these values do not exceed 15% for all cases investigated.

Considering most of the reported literature results in super-resolution reconstruction during the past years, the trend of employing generative artificial intelligence in most branches of science and technology is also driving the super-resolution platforms for fluid dynamics applications, with generative adversarial networks constantly evolving. This is an undoubtedly accurate choice with a high perspective for future implementations. Nonetheless, simpler architectures still have much to offer. Mainly from U-Net basis, these architec-

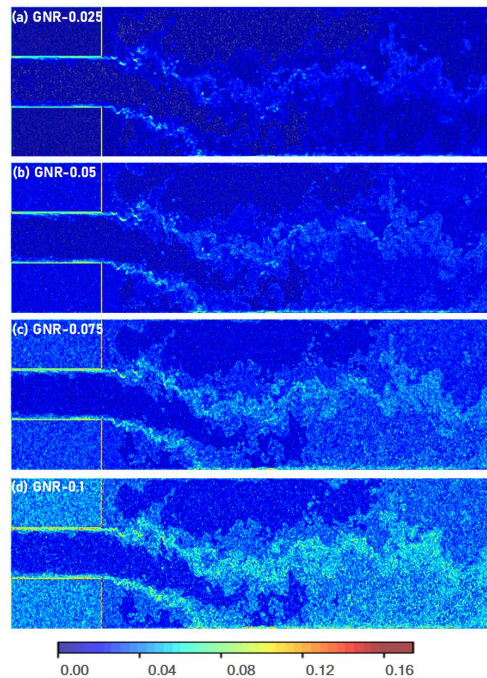


FIG. 11. Error heat maps, denoting the difference between an example HR image and reconstructed images, resulting from a noisy input with Gaussian noise of mean $\mu = 0.0$ and standard deviation: (a) $\sigma = 0.025$, (b) $\sigma = 0.05$, (c) $\sigma = 0.075$, and (d) $\sigma = 0.1$.

tures are practical, run fast, can be easily employed by non-specialists in deep programming techniques, and achieve accurate results in common turbulence phenomena studied.

By comparing DELFI with some well-established super-resolution architectures from the literature, it was found that DELFI achieves higher *PSNR* values for most cases. For example, DELFI's *PSNR* is about 50% higher than the simple SRCNN and 17% higher than the more complex ESRGAN. On the contrary, the MPSRC architecture reaches a 12% higher *PSNR* than DELFI. However, all these values are reported for different datasets, but they are representative of the model's performance in a complex fluid flow application.

The present study also stimulates future research. Specifically, it is worth investigating the model's transferability across cases with limited or unavailable training data and combining experimental and numerical data for training the model. These areas require further research to broaden the application of DELFI and other SR architectures.

ACKNOWLEDGMENTS

This work was supported by computational time granted by the National Infrastructures for Research and Technology SA (GRNET SA) in the National HPC facility - ARIS under project pr013008-AI_PHYSICS.

DATA AVAILABILITY

The data supporting this study's findings are available on request.

REFERENCES

- ¹J. Salvador, *Example-Based super resolution* (Academic Press, 2016).
- ²K. Fukami, K. Fukagata, and K. Taira, "Super-resolution analysis via machine learning: a survey for fluid flows," *Theoretical and Computational Fluid Dynamics* **37**, 421–444 (2023).
- ³H. Gao, L. Sun, and J.-X. Wang, "Super-resolution and denoising of fluid flow using physics-informed convolutional neural networks without high-resolution labels," *Physics of Fluids* **33** (2021).
- ⁴M. F. Fathi, I. Perez-Raya, A. Baghaie, P. Berg, G. Janiga, A. Arzani, and R. M. D'Souza, "Super-resolution and denoising of 4d-flow mri using physics-informed deep neural nets," *Computer methods and programs in biomedicine* **197**, 105729 (2020).
- ⁵A. Pradhan and K. Duraisamy, "Variational multiscale super-resolution: A data-driven approach for reconstruction and predictive modeling of unresolved physics," *International Journal for Numerical Methods in Engineering* **124**, 4339–4370 (2023).
- ⁶F. Sofos, D. Drikakis, I. W. Kokkinakis, and S. M. Spottswood, "Convolutional neural networks for compressible turbulent flow reconstruction," *Physics of Fluids* **35**, 116120 (2023).
- ⁷T. Corpetti, E. Memin, and P. Perez, "Dense estimation of fluid flows," *IEEE Transactions on Pattern Analysis and Machine Intelligence* **24**, 365–380 (2002).
- ⁸L. Zhu, W. Zhang, J. Kou, and Y. Liu, "Machine learning methods for turbulence modeling in subsonic flows around airfoils," *Physics of Fluids* **31**, 015105 (2019).
- ⁹M. Z. Yousif, M. Zhang, L. Yu, R. Vinuesa, and H. Lim, "A transformer-based synthetic-inflow generator for spatially developing turbulent boundary layers," *Journal of Fluid Mechanics* **957**, A6 (2023).
- ¹⁰B. Liu, J. Tang, H. Huang, and X.-Y. Lu, "Deep learning methods for super-resolution reconstruction of turbulent flows," *Physics of Fluids* **32**, 025105 (2020).
- ¹¹H. Kim, J. Kim, S. Won, and C. Lee, "Unsupervised deep learning for super-resolution reconstruction of turbulence," *Journal of Fluid Mechanics* **910**, A29 (2021).
- ¹²A. Guemes, S. Discetti, A. Ianiro, B. Sirmacek, H. Azizpour, and R. Vinuesa, "From coarse wall measurements to turbulent velocity fields through deep learning," *Physics of Fluids* **33**, 075121 (2021).
- ¹³K. Fukami, B. jin An, M. Nohmi, M. Obuchi, and K. Taira, "Machine-learning-based reconstruction of turbulent vortices from sparse pressure sensors in a pump sump," *Journal of Fluids Engineering* (2022).
- ¹⁴A. Kashefi, D. Rempe, and L. J. Guibas, "A point-cloud deep learning framework for prediction of fluid flow fields on irregular geometries," *Physics of Fluids* **33** (2021).
- ¹⁵C. R. Qi, H. Su, K. Mo, and L. J. Guibas, "Pointnet: Deep learning on point sets for 3d classification and segmentation," in *Proceedings of the IEEE conference on computer vision and pattern recognition* (2017) pp. 652–660.
- ¹⁶Y. Du, M. Wang, and T. A. Zaki, "State estimation in minimal turbulent channel flow: a comparative study of 4dvar and pinn," *International Journal of Heat and Fluid Flow* **99**, 109073 (2023).

This is the author's peer reviewed, accepted manuscript. However, the online version of record will be different from this version once it has been copyedited and typeset.

PLEASE CITE THIS ARTICLE AS DOI: 10.1063/5.0200167

Preprint

12

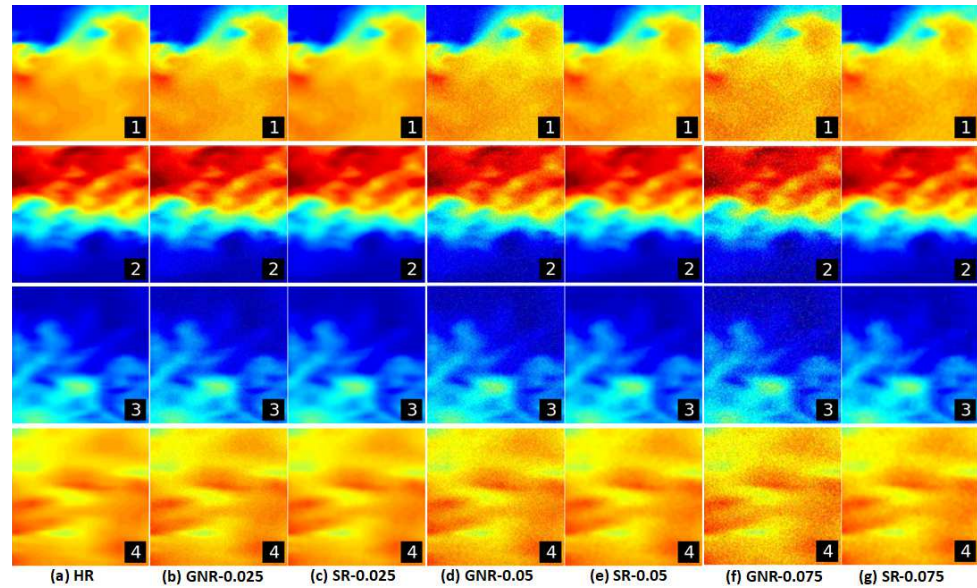


FIG. 12. Flow reconstruction results when the model is trained and validated with images with Gaussian noise, with $\mu = 0.0$ and $\sigma = 0.025 - 0.075$. (a) The ground truth regions of HR resolution are used for reference, and the respective (b) GNR-0.025, (c) GNR-0.025 reconstructed, (d) GNR-0.05, (e) GNR-0.05 reconstructed, (f) GNR-0.075, (g) GNR-0.075 reconstructed.

¹⁷S. Schluter, A. Sheppard, K. Brown, and D. Wildenschild, "Image processing of multiphase images obtained via x-ray microtomography: A review," *Water Resources Research* **50**, 3615–3639 (2014).

¹⁸K. Poulinakis, D. Drikakis, I. W. Kokkinakis, and S. M. Spottswood, "Machine-learning methods on noisy and sparse data," *Mathematics* **11** (2023), 10.3390/math11010236.

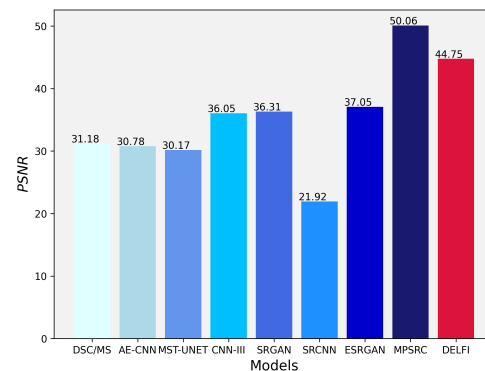


FIG. 13. Comparison of SR models employed for fluid applications regarding the highest PSNR achieved.

¹⁹J. L. Callahan, K. Maeda, and S. L. Brunton, "Robust flow reconstruction from limited measurements via sparse representation," *Physical Review Fluids* **4**, 103907 (2019).

²⁰Z. Luo, L. Wang, J. Xu, M. Chen, J. Yuan, and A. C. C. Tan, "Flow reconstruction from sparse sensors based on reduced-order autoencoder state estimation," *Physics of Fluids* **35**, 075127 (2023).

²¹S. Xu, Z. Sun, R. Huang, D. Guo, G. Yang, and S. Ju, "A practical approach to flow field reconstruction with sparse or incomplete data through physics informed neural network," *Acta Mechanica Sinica* **39**, 322302 (2022).

²²M. Abadi, A. Agarwal, P. Barham, E. Brevdo, Z. Chen, C. Citro, G. S. Corrado, A. Davis, J. Dean, M. Devin, *et al.*, "Tensorflow: A system for large-scale machine learning," arXiv preprint arXiv:1603.04467 (2016).

²³F. Chollet *et al.*, "Keras," <https://keras.io> (2015).

²⁴A. Paszke, S. Gross, F. Massa, A. Lerer, J. Bradbury, G. Chanan, T. Killeen, Z. Lin, N. Gimelshein, L. Antiga, *et al.*, "Pytorch: An imperative style, high-performance deep learning library," *Advances in Neural Information Processing Systems* **32**, 8024–8035 (2019).

²⁵S. Anwar, S. Khan, and N. Barnes, "A deep journey into super-resolution: A survey," *ACM Comput. Surv.* **53** (2020), 10.1145/3390462.

²⁶Z. Wang, J. Chen, and S. C. H. Hoi, "Deep learning for image super-resolution: A survey," *IEEE Transactions on Pattern Analysis and Machine Intelligence* **43**, 3365–3387 (2021).

²⁷T. Falk, D. Mai, R. Bensch, O. Cicek, A. Abdulkadir, Y. Marrakchi, A. Bohm, J. Deubner, Z. Jackel, K. Seiwald, A. Dovzhenko, O. Tietz, C. Dal Bosco, S. Walsh, D. Saltukoglu, T. L. Tay, M. Prinz, K. Palme, M. Simons, I. Diester, T. Brox, and O. Ronneberger, "U-Net: deep learning for cell counting, detection, and morphometry," *Nature Methods* **16**, 67–70 (2019).

²⁸V. Himthani, V. S. Dhaka, M. Kaur, G. Rani, M. Oza, and H.-N. Lee, "Comparative performance assessment of deep learning based image steganography techniques," *Scientific Reports* **12**, 16895 (2022).

²⁹K. He, X. Zhang, S. Ren, and J. Sun, "Deep residual learning for image recognition," in *2016 IEEE Conference on Computer Vision and Pattern*

- Recognition (CVPR)* (2016) pp. 770–778.
- ³⁰A. Krizhevsky, I. Sutskever, and G. E. Hinton, “Imagenet classification with deep convolutional neural networks,” in *Advances in Neural Information Processing Systems*, Vol. 25, edited by F. Pereira, C. Burges, L. Bottou, and K. Weinberger (Curran Associates, Inc., 2012).
- ³¹C. Farabet, C. Couprie, L. Najman, and Y. LeCun, “Learning hierarchical features for scene labeling,” *IEEE Transactions on Pattern Analysis and Machine Intelligence* **35**, 1915–1929 (2013).
- ³²C. Szegedy, W. Liu, Y. Jia, P. Sermanet, S. Reed, D. Anguelov, D. Erhan, V. Vanhoucke, and A. Rabinovich, “Going deeper with convolutions,” in *Proceedings of the IEEE Conference on Computer Vision and Pattern Recognition (CVPR)* (2015).
- ³³G. Hinton, L. Deng, D. Yu, G. E. Dahl, A.-r. Mohamed, N. Jaitly, A. Senior, V. Vanhoucke, P. Nguyen, T. N. Sainath, and B. Kingsbury, “Deep neural networks for acoustic modeling in speech recognition: The shared views of four research groups,” *IEEE Signal Processing Magazine* **29**, 82–97 (2012).
- ³⁴K. Fukami, R. Maulik, N. Ramachandra, K. Fukagata, and K. Taira, “Global field reconstruction from sparse sensors with voronoi tessellation-assisted deep learning,” *Nature Machine Intelligence* **3**, 945–951 (2021).
- ³⁵Z. Deng, C. He, Y. Liu, and K. C. Kim, “Super-resolution reconstruction of turbulent velocity fields using a generative adversarial network-based artificial intelligence framework,” *Physics of Fluids* **31**, 125111 (2019).
- ³⁶D. Drikakis and F. Sofos, “Can artificial intelligence accelerate fluid mechanics research?” *Fluids* **8** (2023), 10.3390/fluids8070212.
- ³⁷X. Wang, K. Yu, S. Wu, J. Gu, Y. Liu, C. Dong, Y. Qiao, and C. Change Loy, “Esrgan: Enhanced super-resolution generative adversarial networks,” in *Proceedings of the European Conference on Computer Vision (ECCV) Workshops* (2018).
- ³⁸J. Kim and C. Lee, “Deep unsupervised learning of turbulence for inflow generation at various reynolds numbers,” *Journal of Computational Physics* **406**, 109216 (2020).
- ³⁹E. Ajuria Illarramendi, M. Bauerheim, and B. Cuenot, “Performance and accuracy assessments of an incompressible fluid solver coupled with a deep convolutional neural network,” *Data-Centric Engineering* **3**, e2 (2022).
- ⁴⁰L. Kong, F. Wang, F. Yang, L. Leng, and H. Zhang, “Fisrcn: a single small-sized image super-resolution convolutional neural network by using edge detection,” *Multimedia Tools and Applications* (2023), 10.1007/s11042-023-15380-3, published online.
- ⁴¹D. Nouri, M. Pasandideh-Fard, M. Javad Oboodi, O. Mahian, and A. Z. Sahin, “Entropy generation analysis of nanofluid flow over a spherical heat source inside a channel with sudden expansion and contraction,” *International Journal of Heat and Mass Transfer* **116**, 1036–1043 (2018).
- ⁴²W. H. Ahmed, C. Y. Ching, and M. Shoukri, “Pressure recovery of two-phase flow across sudden expansions,” *International Journal of Multiphase Flow* **33**, 575–594 (2007).
- ⁴³F. Aloui, L. Doublié, J. Legrand, and M. Souhar, “Bubbly flow in an axisymmetric sudden expansion: Pressure drop, void fraction, wall shear stress, bubble velocities and sizes,” *Experimental Thermal and Fluid Science* **19**, 118–130 (1999).
- ⁴⁴F. Aloui and M. Souhar, “Experimental study of turbulent asymmetric flow in a flat duct symmetric sudden expansion,” *Journal of Fluids Engineering* **122**, 174–177 (2000).
- ⁴⁵D. Drikakis, “Bifurcation phenomena in incompressible sudden expansion flows,” *Physics of Fluids* **9**, 76–87 (1997).
- ⁴⁶R. Wille and H. Fernholz, “Report on the first European mechanics colloquium, on the Coanda effect,” *Journal of Fluid Mechanics* **23**, 801–819 (1965).
- ⁴⁷F. Durst, A. Mellinger, and J. Whitelaw, “Low Reynolds number flow over a plane symmetric sudden expansion,” *Journal of Fluid Mechanics* **64**, 111–128 (1974).
- ⁴⁸R. Fearn, T. Mullin, and K. Cliffe, “Nonlinear flow phenomena in a symmetric sudden expansion,” *Journal of Fluid Mechanics* **211**, 595–608 (1990).
- ⁴⁹N. Moallemi and J. Brinkerhoff, “Numerical analysis of laminar and transitional flow in a planar sudden expansion,” *Computers & Fluids* **140**, 209–221 (2016).
- ⁵⁰K. Karantonis, I. W. Kokkinakis, B. Thornber, and D. Drikakis, “Compressibility in suddenly expanded subsonic flows,” *Physics of Fluids* **33**, 105106 (2021).
- ⁵¹L. Casarsa and P. Giannattasio, “Three-dimensional features of the turbulent flow through a planar sudden expansion,” *Physics of Fluids* **20**, 015103 (2008).
- ⁵²I. W. Kokkinakis, D. Drikakis, K. Ritos, and S. M. Spottswood, “Direct numerical simulation of supersonic flow and acoustics over a compression ramp,” *Physics of Fluids* **32**, 066107 (2020).
- ⁵³E. F. Toro, M. Spruce, and W. Speares, “Restoration of the contact surface in the HLL-Riemann solver,” *Shock Waves* **4**, 25–34 (1994).
- ⁵⁴R. Spiteri and S. Ruuth, “A new class of optimal high-order strong-stability-preserving time discretization methods,” *SIAM Journal on Numerical Analysis* **40**, 469–491 (2002).
- ⁵⁵I. Kokkinakis and D. Drikakis, “Implicit large eddy simulation of weakly-compressible turbulent channel flow,” *Computer Methods in Applied Mechanics and Engineering* **287**, 229–261 (2015).
- ⁵⁶M. Klein, A. Sadiki, and J. Janicka, “A digital filter based generation of inflow data for spatially developing direct numerical or large eddy simulations,” *Journal of Computational Physics* **186**, 652–665 (2003).
- ⁵⁷E. Touber and N. D. Sandham, “Large-eddy simulation of low-frequency unsteadiness in a turbulent shock-induced separation bubble,” *Theoretical and Computational Fluid Dynamics* **23**, 79–107 (2009).
- ⁵⁸J. Hinze, *Turbulence* (McGraw-Hill, 1975).
- ⁵⁹N. J. Georgiadis, D. P. Rizzetta, and C. Fureby, “Large-eddy simulation: current capabilities, recommended practices, and future research,” *AIAA Journal* **48**, 1172–1784 (2010).
- ⁶⁰H. Choi and P. Moin, “Grid-point requirements for large eddy simulation: Chapman’s estimates revisited,” *Physics of Fluids* **24**, 011702 (2012).
- ⁶¹J. Poggie, N. J. Bisek, and R. Gosse, “Resolution effects in compressible, turbulent boundary layer simulations,” *Computers & Fluids* **120**, 57–69 (2015).
- ⁶²A. Khan, A. Sohaail, U. Zahoora, and A. S. Qureshi, “A survey of the recent architectures of deep convolutional neural networks,” *Artificial Intelligence Review* **53**, 5455–5516 (2020).
- ⁶³M. Morimoto, K. Fukami, K. Zhang, A. G. Nair, and K. Fukagata, “Convolutional neural networks for fluid flow analysis: Toward effective metamodelling and low dimensionalization,” *Theoretical and Computational Fluid Dynamics* **35**, 633–658 (2021).
- ⁶⁴S. Albawi, T. A. Mohammed, and S. Al-Zawi, “Understanding of a convolutional neural network,” in *2017 International Conference on Engineering and Technology (ICET)* (2017) pp. 1–6.
- ⁶⁵R. F. Cerqueira and E. E. Paladino, “Development of a deep learning-based image processing technique for bubble pattern recognition and shape reconstruction in dense bubbly flows,” *Chemical Engineering Science* **230**, 116163 (2021).
- ⁶⁶J. Kim, J. K. Lee, and K. M. Lee, “Accurate image super-resolution using very deep convolutional networks,” in *2016 IEEE Conference on Computer Vision and Pattern Recognition (CVPR)* (2016) pp. 1646–1654.
- ⁶⁷V. Nair and G. E. Hinton, “Rectified linear units improve restricted boltzmann machines,” in *Proceedings of the 27th International Conference on International Conference on Machine Learning, ICML’10 (OmniPress, Madison, WI, USA, 2010) p. 807–814.*
- ⁶⁸T. Dai, J. Cai, Y. Zhang, S.-T. Xia, and L. Zhang, “Second-order attention network for single image super-resolution,” in *Proceedings of the IEEE/CVF Conference on Computer Vision and Pattern Recognition (CVPR)* (2019).
- ⁶⁹Y. Tai, J. Yang, and X. Liu, “Image super-resolution via deep recursive residual network,” in *2017 IEEE Conference on Computer Vision and Pattern Recognition (CVPR)* (2017) pp. 2790–2798.
- ⁷⁰J. Gu, X. Sun, Y. Zhang, K. Fu, and L. Wang, “Deep residual squeeze and excitation network for remote sensing image super-resolution,” *Remote Sensing* **11** (2019), 10.3390/rs11151817.
- ⁷¹E. López-Rubio, “Restoration of images corrupted by gaussian and uniform impulsive noise,” *Pattern Recognition* **43**, 1835–1846 (2010).
- ⁷²C. Bonchelet, “Chapter 7 - image noise models,” in *The Essential Guide to Image Processing*, edited by A. Bovik (Academic Press, 2009) pp. 143–167.
- ⁷³H. Qu, T. Feng, Y. Zhang, and Y. Wang, “Ensemble learning with stochastic configuration network for noisy optical fiber vibration signal recognition,” *Sensors* **19** (2019), 10.3390/s19153293.
- ⁷⁴D. Abbott and S. Kline, “Experimental investigation of subsonic turbulent flow over single and double backward facing steps,” *J. Basic Eng* **84**, 317–

This is the author's peer reviewed, accepted manuscript. However, the online version of record will be different from this version once it has been copyedited and typeset.

PLEASE CITE THIS ARTICLE AS DOI: 10.1063/5.0200167

- 325 (1962).
- ⁷⁵P. R. Mehta, "Separated flow through large sudden expansions," *Journal of the Hydraulics Division* **107**, 451–460 (1981).
- ⁷⁶S. De Zilwa, L. Khezzar, and J. Whitelaw, "Flows through plane sudden-expansions," *International Journal for Numerical Methods in Fluids* **32**, 313–329 (2000).
- ⁷⁷M. Escudier, P. Oliveira, and R. Poole, "Turbulent flow through a plane sudden expansion of modest aspect ratio," *Physics of Fluids* **14**, 3641–3654 (2002).
- ⁷⁸C. Kong, J.-T. Chang, Y.-F. Li, and R.-Y. Chen, "Deep learning methods for super-resolution reconstruction of temperature fields in a supersonic combustor," *AIP Advances* **10**, 115021 (2020).
- ⁷⁹K. Fukami, K. Fukagata, and K. Taira, "Super-resolution reconstruction of turbulent flows with machine learning," *Journal of Fluid Mechanics* **870**, 106–120 (2019).
- ⁸⁰K. Fukami, K. Hasegawa, T. Nakamura, M. Morimoto, and K. Fukagata, "Model order reduction with neural networks: Application to laminar and turbulent flows," *SN Computer Science* **2**, 467 (2021).
- ⁸¹K. Bao, X. Zhang, W. Peng, and W. Yao, "Deep learning method for super-resolution reconstruction of the spatio-temporal flow field," *Advances in Aerodynamics* **5**, 19 (2023).
- ⁸²C. Kong, J. Chang, Z. Wang, Y. Li, and W. Bao, "Data-driven super-resolution reconstruction of supersonic flow field by convolutional neural networks," *AIP Advances* **11**, 065321 (2021), https://pubs.aip.org/aip/adv/article-pdf/doi/10.1063/5.0056569/12829225/065321_1_online.pdf.
- ⁸³Y. Jeon and D. You, "Super-resolution reconstruction of transitional boundary layers using a deep neural network," *International Journal of Aeronautical and Space Sciences* **24**, 1015–1031 (2023).
- ⁸⁴C. Dong, C. C. Loy, K. He, and X. Tang, "Learning a deep convolutional network for image super-resolution," in *Computer Vision – ECCV 2014*, edited by D. Fleet, T. Pajdla, B. Schiele, and T. Tuytelaars (Springer International Publishing, Cham, 2014) pp. 184–199.
- ⁸⁵Z. Wang, X. Li, L. Liu, X. Wu, P. Hao, X. Zhang, and F. He, "Deep-learning-based super-resolution reconstruction of high-speed imaging in fluids," *Physics of Fluids* **34**, 037107 (2022), https://pubs.aip.org/aip/pof/article-pdf/doi/10.1063/5.0078644/16642781/037107_1_online.pdf.
- ⁸⁶L. Sun and J.-X. Wang, "Physics-constrained bayesian neural network for fluid flow reconstruction with sparse and noisy data," *Theoretical and Applied Mechanics Letters* **10**, 161–169 (2020).
- ⁸⁷H. Gao, L. Sun, and J.-X. Wang, "Super-resolution and denoising of fluid flow using physics-informed convolutional neural networks without high-resolution labels," *Physics of Fluids* **33**, 073603 (2021).